ELSEVIER

Journal of Quantitative Spectroscopy & Radiative Transfer 103 (2007) 175–192

Journal of Quantitative Spectroscopy & Radiative Transfer

www.elsevier.com/locate/jqsrt

Retrieval of ozone profile from ground-based measurements with polarization: A synthetic study

Xin Guo[a,*], Vijay Natraj[a], Daniel R. Feldman[b], Robert J.D. Spurr[c], Run-Lie Shia[a], Stanley P. Sander[d], Yuk L. Yung[a,b]

[a]*Division of Geological and Planetary Sciences, MC 150-21, California Institute of Technology, 1200 E. California Blvd., Pasadena, CA 91125, USA*

[b]*Division of Engineering and Applied Science, MC 138-78, California Institute of Technology, 1200 E. California Blvd., Pasadena, CA 91125, USA*

[c]*RT SOLUTIONS, Inc., 9 Channing Street, Cambridge, MA 02138, USA*

[d]*Jet Propulsion Laboratory, California Institute of Technology, 4800 Oak Grove Dr., Pasadena, CA 91109, USA*

Received 6 May 2006; received in revised form 27 May 2006; accepted 30 May 2006

Abstract

We perform a retrieval based on optimal estimation theory to retrieve the vertical distribution of ozone from simulated spectra in the Huggins bands. The model atmosphere includes scattering by aerosol as well as Rayleigh scattering. The virtual instrument is ground-based and zenith-viewing. Using this algorithm, we show that it is possible to retrieve the ozone profile provided that the spectral resolution is at least 0.2 nm and the signal to noise ratio greater than 500. Our synthetic retrievals suggest that if we are able to measure the Stokes parameters Q, U and V with accuracy comparable to that of the intensity, the information contained in the measurements, and therefore the inversion, will improve. Furthermore, we find that the measurement of the full Stokes vector from the ground-based instrument will especially enhance the retrieval of tropospheric ozone. Utilizing concepts from information theory, our arguments are confirmed by increases in the degrees of freedom and the Shannon information content in the simulated measurements.

Keywords: Retrieval; Troposphere; Ozone; Polarization; Scattering; Aerosol

1. Introduction

Ozone is one of the major greenhouse gases in the Earth's atmosphere [1,2]. It has been proposed that ozone, especially the lower stratospheric component, can affect the earth's climate significantly [3–6]. Near the surface, ozone can be produced in high concentrations as a result of industrial activities [7,8]. With continuous global industrial growth, the near surface ozone has at least doubled during the last century [9–11]. Therefore,

*Corresponding author. Tel.: +1 626 395 5896; fax: +1 626 585 1917.
E-mail address: xin@gps.caltech.edu (X. Guo).

0022-4073/$ - see front matter © 2006 Elsevier Ltd. All rights reserved.
doi:10.1016/j.jqsrt.2006.05.008

there is an urgent need to quantify ozone variability in the lower stratosphere and the troposphere below the bulk of the ozone layer.

The low concentration of tropospheric ozone beneath the larger concentration of the stratospheric ozone makes it difficult to measure by top of the atmosphere (TOA) based remote sensing techniques. Ground-based measurement therefore becomes a reasonable alternative to TOA ozone profile retrievals. The Umkehr technique is a classical method to derive the ozone vertical distribution from a ground-based instrument. It utilizes the intensity at two wavelengths in the Huggins bands, which is a spectral region with a wide dynamic range of ozone absorption [12]. The Short Umkehr method, which is a modification of the Standard Umkehr method, requires zenith sky measurements of three wavelength pairs instead of one and costs about one third of the observing time [13–15]. However, both methods provide satisfactory ozone abundance only for the stratosphere. Another simple retrieval scheme was performed by Jiang et al. [16] to retrieve the stratospheric and tropospheric column ozone simultaneously. They utilized a least squares method, fitting the downwelling UV radiance at the bottom of the atmosphere (BOA) calculated with a radiative transfer model. In this paper, we retrieve the ozone number density profile at 9 layers (10 levels, see Table 1) from simulated ground-based measurements between 300 and 345 nm. A retrieval method based on optimal estimation theory is applied to solve this inverse problem rigorously. Our observation geometry is similar to that of the Umkehr method. In the standard setup, we use 226 channels to cover the entire spectral region with a 0.2 nm resolution. By doing that, we try to incorporate the information from both strong and weak absorptions in the Huggins bands. Therefore, this retrieval algorithm can be viewed as an extension of the Umkehr method.

Because of the complicated theoretical formulation and engineering issues, polarization is usually ignored in radiative modeling and measurement. However, if we are able to measure the Stokes parameters Q, U and V with accuracy comparable to that of the intensity, the information contained in the observations will increase and the retrieval will be improved. Scattering by air molecules and aerosols polarizes the diffuse radiation [17]. This effect is much stronger in the troposphere than in the stratosphere and the polarized signature will especially constrain the retrieval of tropospheric ozone. The fact that polarization measurements aid the inverse calculation has also been discussed by Hasekamp and Landgraf [18] and Jiang et al. [19]. However, complete ozone profile retrieval has not been done in either work. In this paper, we perform a retrieval of the ozone number density profile, employing forward models both with and without polarization calculations. The results are compared to demonstrate the benefits of using the vector retrieval, i.e. the retrieval with polarization. The use of polarization provides a further extension of the Umkehr technique.

In Section 2, we briefly discuss the radiative transfer theory and introduce a numerical model which calculates the four Stokes parameters of the downwelling radiation at the BOA. In Section 3, we describe the retrieval scheme and compare the retrievals with and without polarization. Simple sensitivity studies are also presented in this section. In Section 4, we use information theory to test the quality of the inversion and calculate the increase in information content from incorporating the polarization. Conclusions and discussions are presented in Section 5.

Table 1
The standard profiles for the forward model

Layer number	Height (km)	Temperature (K)	Atmospheric number density (m^{-3})	Aerosol number density (m^{-3})	Ozone number density (m^{-3})
1	0–2.50	280.0	2.35×10^{25}	4.37×10^{8}	7.94×10^{17}
2	2.50–4.85	264.3	1.88×10^{25}	6.82×10^{6}	1.49×10^{18}
3	4.85–6.41	251.6	1.52×10^{25}	8.02×10^{5}	1.57×10^{18}
4	6.41–9.70	235.8	1.17×10^{25}	4.67×10^{5}	1.94×10^{18}
5	9.70–11.3	221.0	8.75×10^{24}	3.80×10^{5}	2.74×10^{18}
6	11.3–18.6	216.7	5.19×10^{24}	5.80×10^{5}	4.51×10^{18}
7	18.6–21.0	217.1	2.05×10^{24}	7.84×10^{5}	6.30×10^{18}
8	21.0–27.4	220.7	1.11×10^{24}	4.22×10^{5}	5.92×10^{18}
9	27.4–48.4	247.2	3.01×10^{23}	2.50×10^{4}	2.61×10^{18}

2. Radiative transfer model with scattering

2.1. Theory of radiative transfer

The equation of radiative transfer can be written as [20]

$$u\frac{\partial}{\partial\tau}\mathbf{I}(\tau,u,\varphi)=\mathbf{I}(\tau,u,\varphi)-\mathbf{J}(\tau,u,\varphi) \tag{1}$$

in the absence of thermal emission. $\mathbf{I}$ is the diffuse (excluding the direct solar beam) radiance vector, which consists of Stokes parameters [20] I, Q, U and V as its components. τ, u and φ denote the optical thickness (measured downward from the upper boundary), the cosine of the polar angle (defined to be positive in the upper hemisphere) and the azimuthal angle (measured counterclockwise, looking down, from an arbitrary but fixed direction), respectively. The source term $\mathbf{J}$ has the form

$$\mathbf{J}(\tau,u,\varphi)=\frac{\omega(\tau)}{4\pi}\int_{-1}^{1}\int_{0}^{2\pi}\mathbf{P}(u,u',\varphi-\varphi')\,\mathbf{I}(\tau,u',\varphi')\,\mathrm{d}\varphi'\,\mathrm{d}u'+\mathbf{Q}(\tau,u,\varphi), \tag{2}$$

where ω denotes the single scattering albedo and $\mathbf{P}$ is called the phase matrix, which is related to the Mueller matrix and the scattering matrix. The former is the linear transformation connecting the incident and (singly) scattered Stokes vectors in the scattering plane. For scattering by a small volume containing an ensemble of particles, the ensemble-averaged Mueller matrix is called the scattering matrix. When transforming from the scattering plane to a fixed frame (typically the local meridian plane), we obtain the phase matrix. We restrict our attention to scattering matrices of the form considered by Hovenier [21]. This type with only six independent elements is valid in the following situations [22]:

(a) scattering by an ensemble of randomly oriented particles, each with a plane of symmetry,
(b) scattering by an ensemble of particles and their mirror particles in equal number and random orientation,
(c) Rayleigh scattering.

The first term on the right hand side of Eq. (2) accounts for the integrated scattering of the diffuse light from all directions into the viewing direction and the inhomogeneous term $\mathbf{Q}$ describes single scattering of the attenuated direct solar beam. This term can be expressed as [23]

$$\mathbf{Q}(\tau,u,\phi)=\frac{\omega}{4\pi}\mathbf{P}(u,-\mu_0,\phi-\phi_0)\mathbf{I}_0\,\mathrm{e}^{-\tau_{\mathrm{sph}}(\tau)}, \tag{3}$$

where τ_{sph} is the slant optical path, $\mu_0=|u_0|$ and $\mathbf{I}_0$ is the Stokes vector of the incoming solar beam. This so called pseudo-spherical formulation is designed to allow for sphericity due to the earth's curvature, especially at high solar zenith angles. The attenuation of the direct solar beam is computed in a spherical-shell atmosphere, but line-of-sight attenuation and all scattering events continue to be treated for a plane-parallel medium. Note that for a plane-parallel atmosphere $\tau_{\mathrm{sph}}=\tau/\mu_0$.

We seek a solution to Eq. (1), subject to the TOA (no downwelling diffuse radiance) and surface (prescribed bidirectional reflectance) boundary conditions, and continuity at the layer interfaces. The total radiance vector is the sum of the diffuse and direct components, where the direct radiance vector $\mathbf{I}^{\mathrm{dir}}$ is given by

$$\mathbf{I}^{\mathrm{dir}}(\tau,u,\phi)=\mathbf{I}_0\mathrm{e}^{-\tau_{\mathrm{sph}}(\tau)}\delta(u-u_0)\delta(\phi-\phi_0), \tag{4}$$

where δ is the Dirac delta function.

2.2. Radiative model

In this work, we use the linearized vector radiative transfer model VLIDORT [24,25] for the numerical computation of the Stokes vector in a multiply scattering multilayer medium. This model uses the discrete ordinate method to approximate the multiple scatter integrals. VLIDORT has the pseudo-spherical capability. VLIDORT is also fully linearized: along with the polarized radiance field, it will deliver analytic weighting functions with respect to any atmospheric and/or surface properties. This linearization facility is very useful

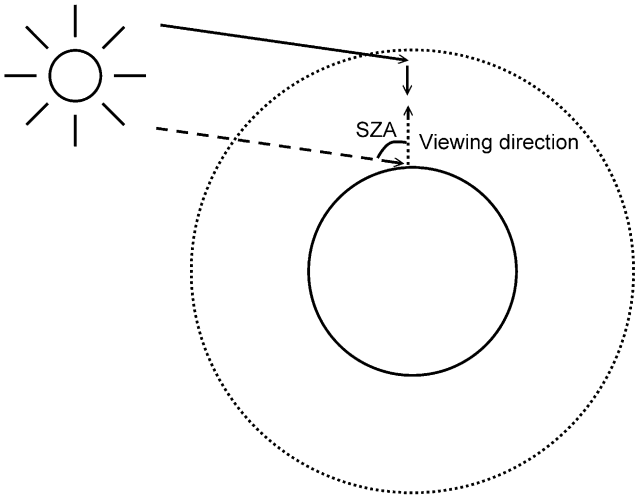

Fig. 1. Geometry of the model. The virtual instrument looks at the zenith and measures the scattered light. The direct incoming solar beam and the line of sight are in the same plane, which is perpendicular to the surface.

for the generation of ozone profile weighting functions in the present work (see Section 3.1). VLIDORT has been validated against Rayleigh [26] and aerosol benchmark results [27], and also against the pseudo-spherical TOMRAD model [28] for the present application involving ozone absorption and Rayleigh scattering for a ground-based retrieval scenario.

Fig. 1 shows the viewing geometry of the radiative model. The solar zenith angle (SZA) is 81.1° and the relative azimuthal angle (the difference between the azimuthal angles of the line of sight and the incoming sunlight) is 0°. The virtual instrument is located at the BOA and looks upwards at the zenith. The sky is assumed to be cloud-free. Optical properties are generated by a radiative transfer model described by Michelangeli et al. [29] and Jiang et al. [16]. Vertical profiles of temperature and air molecule number density from the 1976 US Standard Atmosphere are incorporated as the standard background profiles. We use the standard aerosol profile described by Demerjian et al. [30]. The aerosol particles were chosen to be randomly oriented oblate spheroids with aspect ratio 1.999987, size parameter 3 and index of refraction $1.53-0.006i$. The above aerosol type was chosen because the expansion coefficients for such a model have been computed to very high accuracy by Kuik et al. [31]. We retrieve the ozone number density in nine layers (the model atmosphere has 10 levels, whose altitudes are shown in Table 1). In each layer, the number densities of air molecules, ozone molecules, aerosols, etc. are linearly interpolated between the values at the two boundary levels. The column integrated optical depths of various extinction processes in the model are shown in Fig. 2. VLIDORT is used to generate the transmittance spectra at the surface to cover the Huggins bands (300–345 nm) with adjustable spectral resolution. Inelastic scattering (Ring effect) is not included. We do not distinguish the transmittance (or the reflectance) spectrum from the corresponding radiance spectrum in the following discussion because they only differ by a constant spectrum, viz., that of the sun. For the rest of this paper, we assume that we know the solar spectrum perfectly.

3. Retrieval methodology and results

3.1. Retrieval theory and Levenberg–Marquardt iteration

The forward model is described by

$$\mathbf{y} = F(\mathbf{x}), \tag{5}$$

where $\mathbf{x}$ is the state vector (number density profile of ozone in this case), F refers to the forward model and $\mathbf{y}$ is the theoretical radiance corresponding to the state $\mathbf{x}$. For instance, the formulation described in Section 2 is a

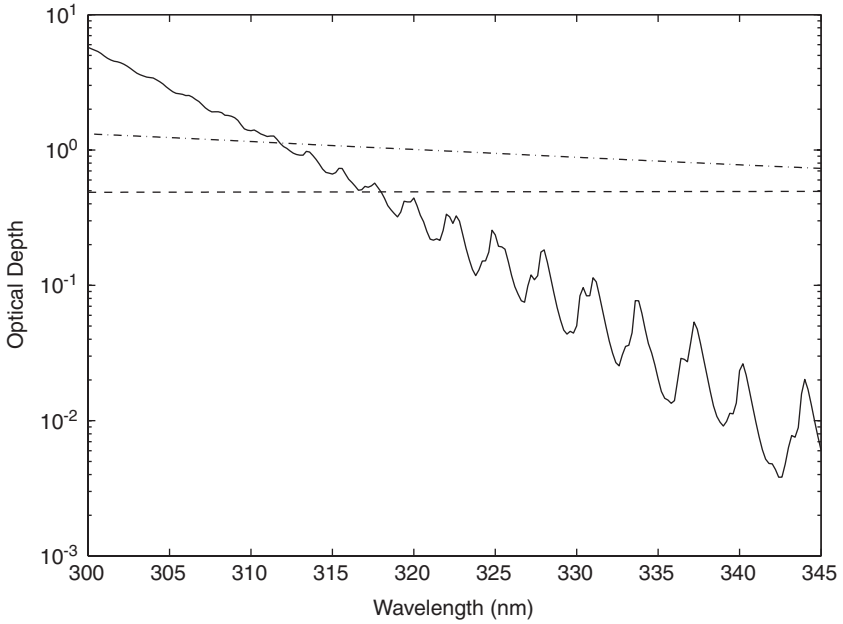

Fig. 2. Column integrated extinction optical depths. Dashed line: aerosol extinction; dash–dotted line: Rayleigh scattering; solid line: ozone extinction.

forward model. A retrieval method is applied in order to solve the inverse problem, i.e. retrieve $\mathbf{x}$ from $\mathbf{y}$ [1,32]. Much work has been devoted to the development of theories that detail the translation of remote sensing radiance measurements to descriptions of the atmospheric state. The remotely measured spectrum represents a Fredholm Integral of the First Kind that describes atmospheric interactions and this class of problems can be notoriously difficult to constrain. The weighting function ($\mathbf{K}$, also known as Kernel, Jacobian, etc.) is the Fréchet derivative of the forward model with respect to the state vector. The elements of $\mathbf{K}$ are defined as

$$K_{jk} = \frac{\partial F_j(\mathbf{x})}{\partial x_k}, \tag{6}$$

where j is the index of the wavelength channel and k is the index of the altitude level. In a linear regime, the weighting function adequately describes the response of the forward model to expected perturbations in the atmospheric state. In a moderately linear regime, the weighting function matrix varies smoothly and slowly with perturbations in the atmospheric state. The standard approach for atmospheric retrievals involves finding the solutions in a moderately linear regime. A solution in an optimization sense involves minimizing a cost function that sufficiently describes the balance between prior understanding of the state and understanding of the measurement and its associated uncertainty. In this case, the cost function is a weighted measure of the discrepancy between the current state vector and the *a priori*, plus the difference between the radiances corresponding to the current state vector and the observation. The cost function χ^2 is defined as

$$\chi^2 = [\mathbf{x}_\mathrm{a} - \mathbf{x}]^\mathrm{T}\mathbf{S}_\mathrm{a}^{-1}[\mathbf{x}_\mathrm{a} - \mathbf{x}] + [\mathbf{y}_\mathrm{O} - F(\mathbf{x})]^\mathrm{T}\mathbf{S}_\varepsilon^{-1}[\mathbf{y}_\mathrm{O} - F(\mathbf{x})], \tag{7}$$

where $\mathbf{y}_\mathrm{O}$ is the observed radiance, $\mathbf{x}$ is the current state vector, $\mathbf{x}_\mathrm{a}$ is the *a priori* state vector, which describes our previous knowledge about the atmospheric state we want to retrieve, $\mathbf{S}_\mathrm{a}$ is the *a priori* covariance matrix, and $\mathbf{S}_\varepsilon$ is the measurement error covariance matrix.

Our retrieval routine follows the Levenberg–Marquardt (L–M hereafter) iteration method suggested by Rodgers [32]. The L–M method is an optimization routine which iteratively finds the solution that minimizes the cost function. The L–M iteration gives

$$\mathbf{x}_{i+1} = \mathbf{x}_i + \left[(1+\gamma)\mathbf{S}_\mathrm{a}^{-1} + \mathbf{K}^\mathrm{T}\mathbf{S}_\varepsilon^{-1}\mathbf{K}\right]^{-1}\left\{\mathbf{K}^\mathrm{T}\mathbf{S}_\varepsilon^{-1}\left[\mathbf{y}_\mathrm{O} - F(\mathbf{x}_i)\right] - \mathbf{S}_\mathrm{a}^{-1}[\mathbf{x}_i - \mathbf{x}_\mathrm{a}]\right\}, \tag{8}$$

where $\mathbf{x}_i$ is the state vector before the ith iteration, $\mathbf{x}_{i+1}$ is the state vector after the ith iteration and before the i+1st iteration, $\mathbf{K}$ is the weighting function for the ith iteration, and γ is a hybridization parameter which varies between 0 (Gauss–Newton iteration) and a large value (steepest descent update). The iteration ideally terminates when the cost function reaches a minimum, at which point the retrieval algorithm will produce an unbiased final state vector and a radiance vector that incorporates the maximum information known about the state both from the prior knowledge and from the measurement.

The L–M optimization method is chosen because it generally finds the cost-function minimum with few iterations and can navigate non-trivial and even moderately non-linear cost-function surfaces. The performance of the optimization algorithm can be highly dependent on a proper initial choice and update schemes for the hybridization parameter.

The total retrieval error covariance matrix in the linear or moderately non-linear regime is

$$\hat{\mathbf{S}} = \left(\mathbf{K}^{\mathrm{T}}\mathbf{S}_{\varepsilon}^{-1}\mathbf{K} + \mathbf{S}_{\mathrm{a}}^{-1}\right)^{-1}. \tag{9}$$

However, a covariance matrix as a description of the error of a measurement is not easy to visualize. The simplest component of the error is the variance, i.e. the diagonal elements of the covariance matrix, and this is often the only error description that is presented with a retrieval [32].

3.2. Synthetic retrieval setup

The monthly mean ozone number density profile in December 1997 at the location of the Jet Propulsion Laboratory, table mountain facility (TMF, 34.4°N, 117.7°W), was obtained from the European Centre for Medium-Range Weather Forecasts (ECMWF) reanalysis ERA-40 dataset [33] and used as the *a priori* state vector ($\mathbf{x}_{\mathrm{a}}$). We generate the radiance spectrum using the forward model described in Section 2.

$$\mathbf{y}_{\mathrm{t}} = F(\mathbf{x}_{\mathrm{t}}), \tag{10}$$

where $\mathbf{x}_{\mathrm{t}}$ refers to the "true" state that we want to retrieve and $\mathbf{y}_{\mathrm{t}}$ corresponds to the "true" radiance (without noise). Random noise $\boldsymbol{\varepsilon}$ is added to the "true" spectrum to simulate the actual measurement $\mathbf{y}_{\mathrm{O}}$.

$$\mathbf{y}_{\mathrm{O}} = \mathbf{y}_{\mathrm{t}}(1 + \varepsilon). \tag{11}$$

The noise spectrum ($\boldsymbol{\varepsilon}$) has a standard deviation equal to the inverse of the signal-to-noise ratio (SNR). We assume that the errors in different channels are uncorrelated and uniform, leading to a diagonal error covariance matrix ($\mathbf{S}_{\varepsilon}$), whose components are equal to SNR^{-2}. We construct the *a priori* covariance matrix ($\mathbf{S}_{\mathrm{a}}$) from the ECMWF dataset [33], and test the code with the synthetic observations ($\mathbf{y}_{\mathrm{O}}$) and a starting state vector $\mathbf{x}_0 = 1.01 \times \mathbf{x}_{\mathrm{a}}$. We use a relatively small perturbation for the initial guess because we do not know whether the inversion is stable and sufficiently linear near this *a priori*. The weighting function matrix ($\mathbf{K}$) is calculated using Eq. (6) in this *a priori* regime. In order to avoid singularities, the state vector and radiance spectrum are scaled by reference vectors ($\mathbf{x}_{\mathrm{r}}$ and $\mathbf{y}_{\mathrm{r}}$, where $\mathbf{y}_{\mathrm{r}} = F(\mathbf{x}_{\mathrm{r}})$). The retrieval code successively updates the state vector and synthetic radiance after each step until convergence is obtained. The state vector is expected to approach the "true" state.

Standard model output spectra are shown in Fig. 3. The dashed and solid lines show the Stokes parameter I of the downwelling radiance at the BOA for the scalar and vector models, respectively, while the dash–dotted line shows the Stokes parameter Q. There are obvious differences between the intensity outputs from the scalar model and the vector model. This discrepancy is consistent with Lacis et al. [34]. We perform both scalar and vector retrievals with spectra covering the entire Huggins bands (300–345 nm) with a 0.2 nm resolution. For our scalar retrieval model, we only consider Stokes parameter I in the forward calculation and retrieval. While for our vector retrieval model, we use all four Stokes parameters. For observations in the principal plane, U and V should be identically zero for unpolarized incident light. Therefore, we simply neglect the latter two components in the vector forward model and retrieval. Comparisons of the results from the scalar and vector inversions are described below.

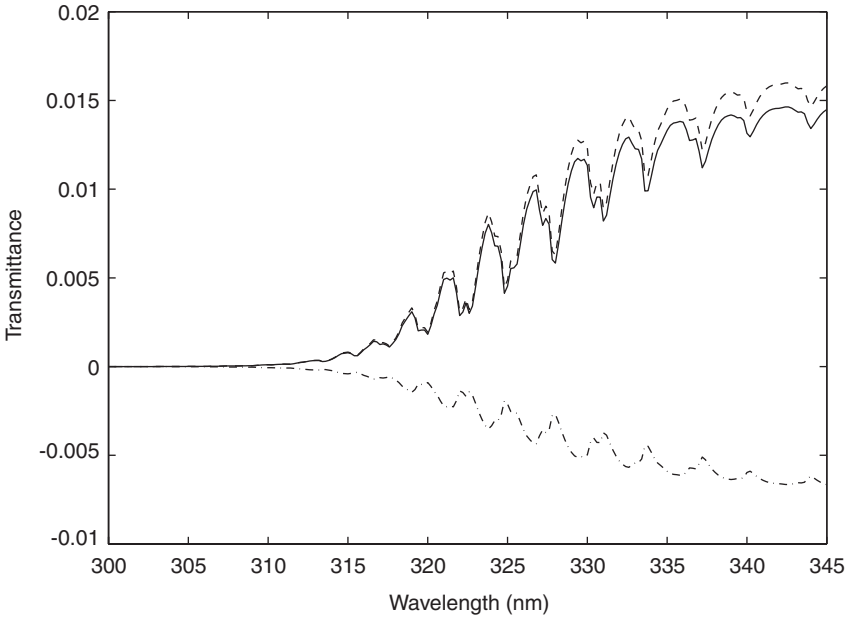

Fig. 3. Stokes parameters computed by the forward models. Dashed line: I (scalar); solid line: I (vector); dash–dotted line: Q.

3.3. Synthetic retrieval results

Since we do not know *a priori* that the inversion is stable and sufficiently linear in the regime of the solution, we compare the scalar and vector retrievals statistically. We run both retrievals 20 times, with the same setup but different random noise values at the same expected SNR (SNR = 1000). The synthetic retrievals were run 20 times because of computation time limitations, but the qualitative behavior of the results is not expected to change much by performing more runs. The nine layer profiles are compared in the following analysis.

Fig. 4 shows the ozone number density profiles. The squares and diamonds show the mean retrieved number density profile for the scalar and vector retrievals respectively, and the solid line indicates the "true" profile. The two mean retrieved states and the "true" state overlap with one another, which suggest that both inversions tend to approach the "true" state.

In order to bring out the difference between the retrieved and the "true" states, we plot the mean profiles (solid lines) for the scalar and vector models, scaled by the reference state, in Figs. 5(a) and (c), respectively. The straight dashed lines correspond to the "true" state in both plots. The discrepancy between the "true" and retrieved states is small (less than 0.5%) above 15 km, where the ozone is denser. The difference is larger (as big as 1.5%) in the troposphere, where the ozone concentration is much lower. We have qualitatively anticipated this pattern in Section 1. Considering the relatively small number of runs, we expect that the inversion algorithm, both with and without polarization, will eventually yield unbiased ozone profiles from synthetic observations.

Error bars calculated using Eq. (9) and the standard deviations of the retrieved states are shown in Figs. 5(b) and (d), for the scalar and vector models, respectively. The straight dashed lines in both plots indicate the "true" state. Close to the surface, the standard deviation and error bars are relatively large. This is a consequence of the Lambertian surface that we use in the forward model. The Lambertian surface depolarizes the reflected light and therefore reduces the information contributed by the polarization, especially at the surface. Another error source is the *a priori* covariance matrix, which is derived from the ECMWF ozone output in the pressure coordinate. ECMWF ozone data in the troposphere is known to be biased, and has large variance [33]. Error in the boundary layer is also introduced by the interpolation and extrapolation to the altitude coordinate using assumptions of constant scale height and surface pressure. The error in the covariance matrix will be transferred to the retrieved concentration. On the other hand, there is a sharp

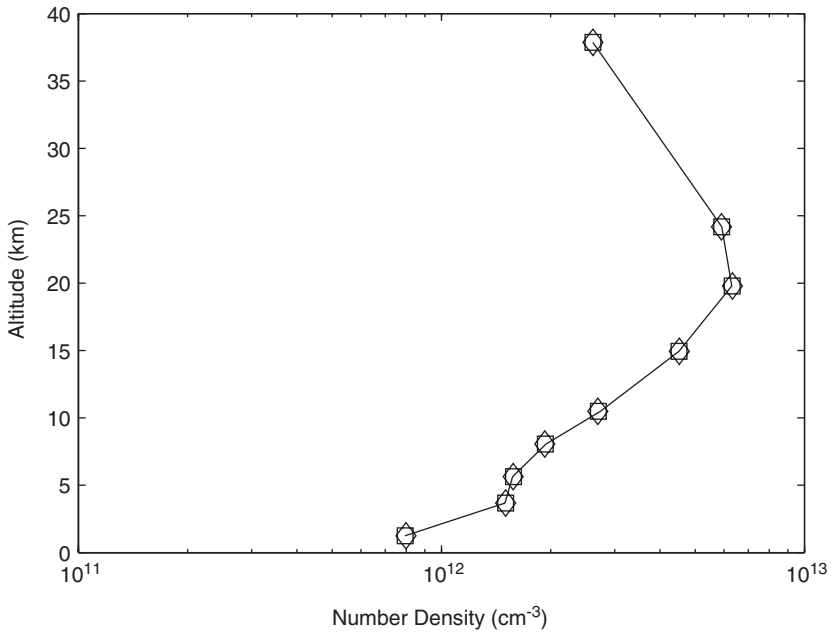

Fig. 4. Ozone number density profiles. Squares: mean retrieved profile (scalar); diamonds: mean retrieved profile (vector); solid line: "true" state.

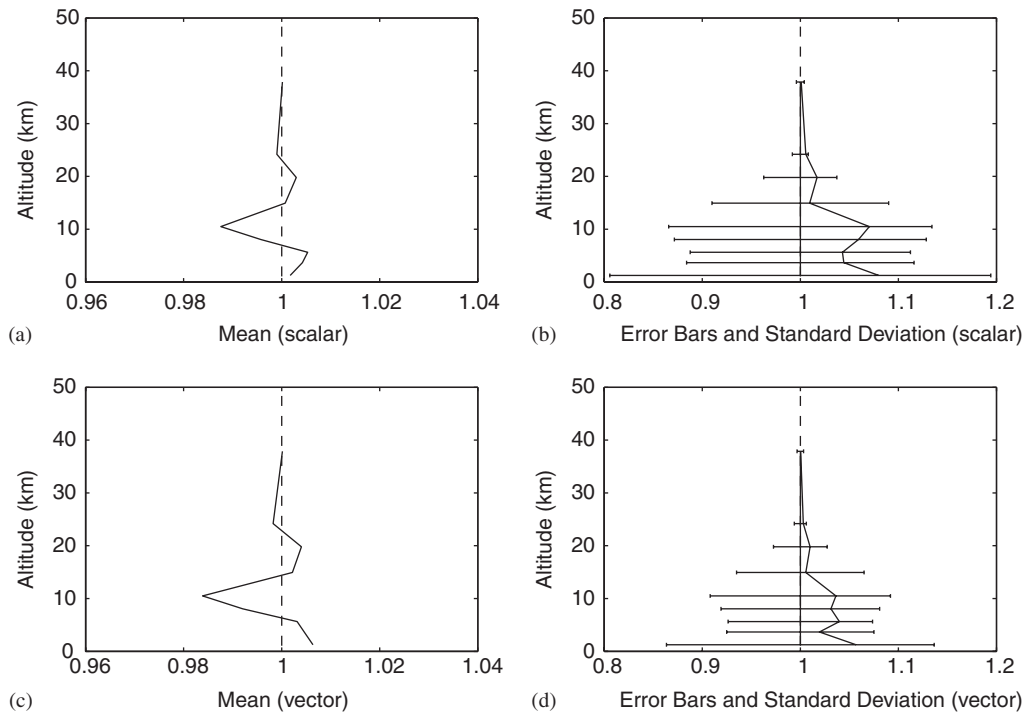

Fig. 5. Scaled profiles, error bars and standard deviation. The dashed line corresponds to the "true" state. (a) Mean retrieved state of the scalar model scaled by the reference state. (b) Standard deviation and error bars of the scalar model. (c) Mean retrieved state of the vector model scaled by the reference state. (d) Standard deviation and error bars of the vector model.

decrease in the ozone concentration at the boundary. Even if the large scaled standard deviation at the ground level is realistic, the variation in number density, which is the product of the scaled standard deviation and the reference number density, is consistent in the troposphere. In practice, it is reasonable to make an in-situ measurement of ozone at the surface to constrain the remote sensing.

In both Figs. 5(b) and (d), small standard deviations (less than 2%) are found in the stratosphere, while relatively large (5–10% at most altitudes) standard deviations are seen in the lower atmosphere. In other words, the difference between the retrieved state and the "true" state is small in the stratosphere and relatively large in the troposphere. The error bars and the standard deviation are generally consistent with each other and close to the prediction from Section 1.

It is important to point out the improvement from the scalar inversion. For each synthetic retrieval, SNR is controlled but the random noise in each channel is unknown, which mimics actual situations. The standard deviation characterizes the difference between the retrieved state and the expected state (the "true" state) for a retrieval done without knowing the exact noise pattern in the measurement. Therefore, the standard deviation profiles are adequate evaluations of the inversion model quality. As seen in Figs. 5(b) and (d), the vector retrieval model does not show significant improvement in the stratosphere, while in the troposphere, obvious decreases (up to 3.4%) in retrieved standard deviation appear at various altitudes. In other words, the retrieved tropospheric ozone from the vector model is closer to the "true" state than that from the scalar model. Similar advantages can be seen from the error bars. The decrease in standard deviation and error bars suggests that the introduction of polarization in the measurement and inversion will improve the quality of ozone retrieval in the troposphere.

Another way to evaluate the quality of the retrieval is to compare the observed radiance with that corresponding to the retrieved state. Since we generate the synthetic spectrum with a known forward model, we know the "true" radiance ($\mathbf{y}_t$). We subtract the "true" spectrum from the radiance to get the residual spectrum ($\mathbf{y}_{res}$) after the last iteration.

$$\mathbf{y}_{res} = \mathbf{y}_f - \mathbf{y}_t, \tag{12}$$

where $\mathbf{y}_f$ refers to the spectrum corresponding to the retrieved state. The residual spectrum indicates how close the radiance corresponding to the final state is to that of the "true" state. Fig. 6(a) shows the mean residual spectra ($\mathbf{y}_{res}$) for the scalar (dashed line) and vector (solid line) models. In our experiment, the virtual instrumental noise is assumed to be 0.1%. After the last iteration, both inversions have a maximum residual of 0.01% and less than 0.002% on average. Some of the absorption features of ozone remain in the residual spectrum simply due to the imperfection of the retrieval. In practice, the "true" spectrum is unknown and a practical residual is therefore often defined as

$$\mathbf{y}^{p}_{res} = \mathbf{y}_f - \mathbf{y}_O = \mathbf{y}_{res} - \varepsilon. \tag{13}$$

In our retrieval results, $\mathbf{y}_{res}$ is at least an order of magnitude smaller than the noise, and we expect that there is only random noise left in the practical residual spectra when the inversion algorithm converges. Fig. 6(b) shows the standard deviation of the residuals for the scalar (dashed line) and vector (solid line) models. The standard deviation spectrum of the vector model is closer to zero than that of the scalar model, which suggests the vector model will generate a final state whose spectra is closer to the "true" state.

The ozone cross section is very sensitive to temperature change [16,35]. The relatively high ozone concentration in the stratosphere, along with the large temperature variation, gives rise to large optical depth variation in the stratosphere. The downwelling radiance change at the surface is thus dominated by the ozone concentration change in the stratosphere compared to that in the troposphere. In other words, the inverse calculation of stratospheric ozone from remote sensing with this viewing geometry is well constrained by the downwelling intensity. Fig. 7(a) shows the variation in the downwelling intensity received at the BOA after perturbing the ozone number density by 1% at different altitudes (essentially the weighting function for the intensity defined by Eq. (6), Fig. 8(a) shows the normalized weighting function profile for the intensity of three different wavelengths). Stratospheric ozone changes dominate the variance in this spectral region, and the most prominent feature corresponds to the perturbation made between 20 and 25 km, where the ozone concentration peaks.

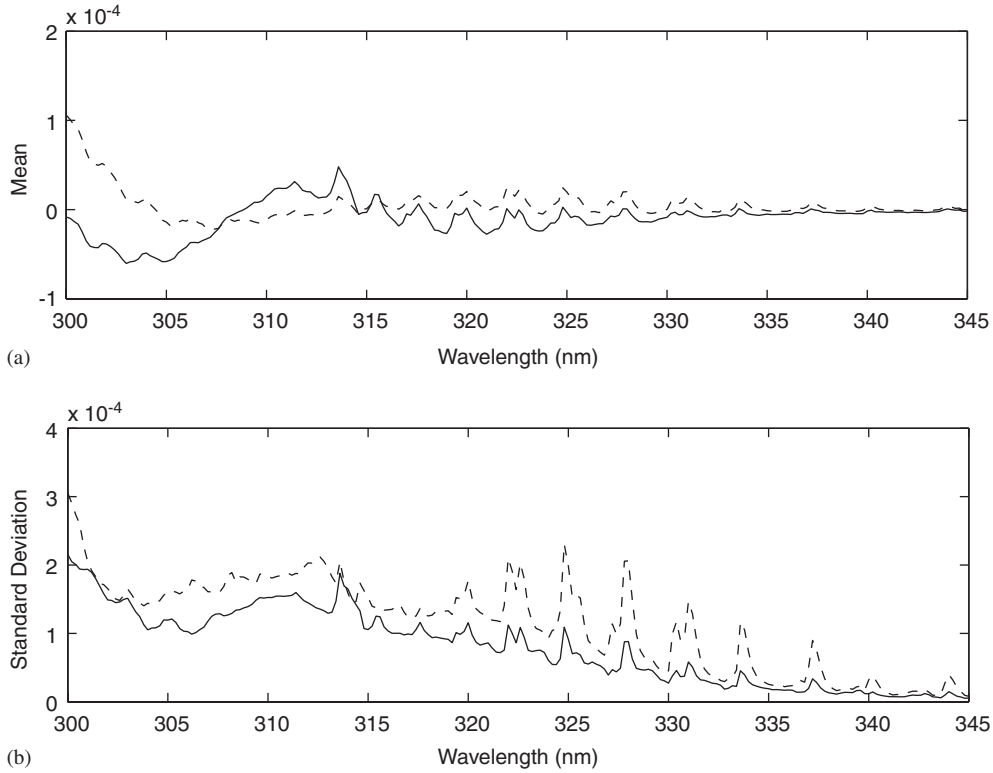

Fig. 6. Residual spectra (intensity only) scaled by that corresponding to the *a priori*. (a) Mean residual spectra. Dashed line: scalar; solid line: vector. (b) Standard deviation spectra. Dashed line: scalar; solid line: vector.

On the other hand, scattering by aerosols and atmospheric molecules polarizes the radiance. In the upper atmosphere, the scattering species are so sparse that the polarization signatures are negligible, while in the troposphere, scattered light is heavily polarized because of the high concentration of the aerosols and air molecules. Hence, the polarization signature received by the ground-based instrument comes primarily from the troposphere. Since we fix the aerosol and atmospheric number density profiles, changes in the observed polarization state are entirely due to variations in the tropospheric ozone. We therefore expect that the extra measurements of Q, U and V will aid the inversion of ozone in the troposphere. We introduce the degree of polarization (DoP) to demonstrate the polarization signature contrast. The DoP is defined as

$$\frac{\left(Q^2+U^2+V^2\right)^{1/2}}{I}. \tag{14}$$

It is a metric for the polarization content of light. Fig. 7(b) shows the DoP change of the measurements made at the BOA after perturbing ozone by one Dobson Unit (DU) at different levels (essentially the weighting function for the DoP, instead of the intensity, as defined by Eq. (6). Fig. 8(b) shows the normalized weighting function profile for the DoP of three different wavelengths). The major variation of the DoP for all the wavelengths results from changes that occurred below 20 km, which suggests sensitivity to the tropospheric ozone embedded in the polarization signal. The ozone below 10 km impacts the DoP most significantly.

3.4. Sensitivity studies

3.4.1. Aerosol (dust)

Aerosol loading is highly variable in the lower atmosphere and can significantly affect remote sensing. In order to test the robustness of our retrieval method over the TMF region, we perform experiments with

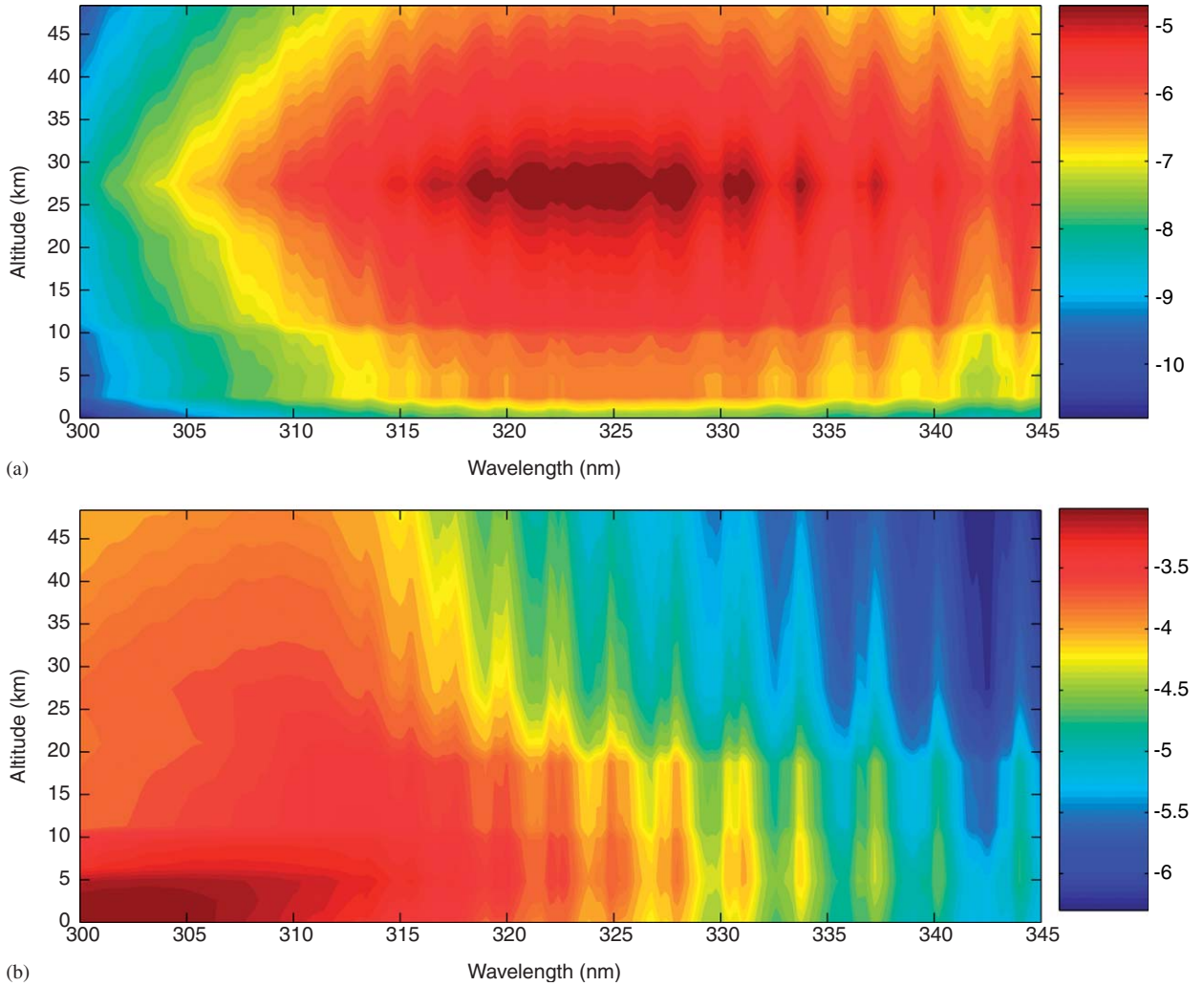

Fig. 7. Intensity and DoP weighting function ($\log_{10}$ scale) matrix. (a) Change of intensity at the BOA, if the ozone number density is perturbed by 1% at different altitudes. (b) Change of DoP at the BOA, if ozone number abundance is perturbed by 1 DU at different altitudes.

various dust profiles. We use climatology aerosol output near the TMF region from the model of atmospheric transport and chemistry (MATCH) [36] (the closest output grid point is at 35.2°N, 118.1°W). The model generates dust mass mixing ratio profiles in four size distribution bins. For simplicity, we convert the total monthly mean mass mixing ratio of the four bins to number density assuming the dust particles to be spherical with radius of 0.07 micron and single scattering albedo 0.99. We test the scalar and vector retrievals based on three climatology dust profiles: the annual average, the maximum (April) and the minimum (August).

Fig. 9 shows the results of this sensitivity study. Mean retrieved states (scaled by the reference state) of the scalar and vector models are shown in Figs. 9(a) and (c), respectively; the corresponding standard deviations are shown in Figs. 9(b) and (d). In each plot, different line styles are used to indicate the results for different dust concentrations (solid line: the standard dust profile described in Section 2; dashed line: the annual mean of the climatology data; dash–dotted line: the maximum; dotted line: the minimum; straight dashed line: "true" state).

As has already been discussed, there is a large error close to the surface. At other altitudes, the error of the retrieved mean profiles for different dust loading is less than 3% for the scalar model and less than 1% for the vector model. Though the scalar model has slightly worse average profile and the vector model provides

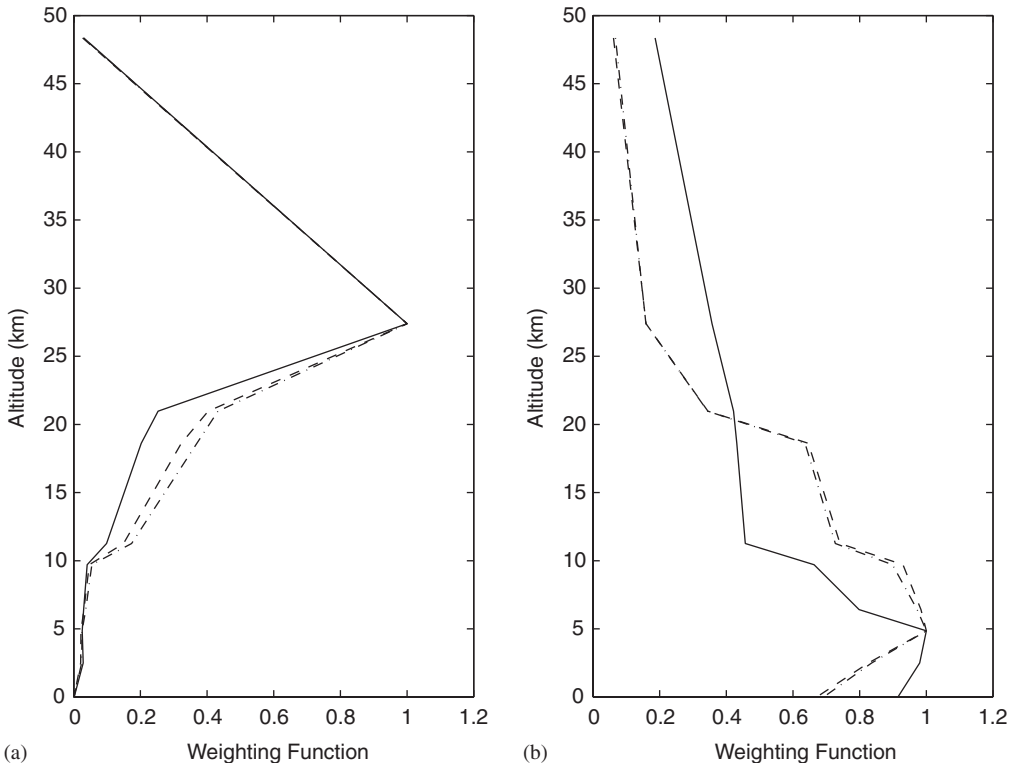

Fig. 8. Normalized weighting function profiles and for different wavelengths. (a) Same as Fig. 7(a), for different wavelengths. Solid line: 310 nm; dashed line: 325 nm; dash–dotted line: 340 nm. (b) Same as Fig. 7(b), for different wavelengths. Solid line: 310 nm; dashed line: 325 nm; dash–dotted line: 340 nm.

slightly better results compared to the standard dust loading case, it is reasonable to expect that both models will eventually yield the correct result. Moreover, for both scalar and vector retrievals, there is no apparent discrepancy among different standard deviation profiles, which overlap with one another in Figs. 9(b) and (d). We conclude that heavier dust loading does not adversely affect the retrieval of ozone with this algorithm, at least not for the retrieval at TMF.

3.4.2. SNR versus number of channels

Current grating instruments usually have SNR 200–300, which is much lower than what we assume in the synthetic retrieval. For grating instruments, there is a trade-off between SNR and number of channels (spectral resolution). For instance, SNR values of 1000 or higher can be achieved by adopting wider channels while covering the same spectral region. The following experiment is performed to show the effect of broader channel width with higher SNR. We input the 0.2 nm resolution spectra to a square wave convolution function with half width 0.5 nm and generate 1 nm resolution spectra. SNR of the coarser resolution spectrum should be several times larger than that of the 0.2 nm resolution spectrum. Therefore, the SNR of the new spectra is still assumed to be 1000. Such a simulated instrument is an idealized substitution of a 0.2 nm detector limited device (SNR is proportional to the number of photons received in each wavelength pixel) with SNR = 200 or a 0.2 nm background limited device (SNR is proportional to the square root of the number of photons) with SNR = 447.

Fig. 10 shows the scaled profiles and standard deviation. The straight dashed lines correspond to the ''true'' state. Figs. 10(a) and (c) show the mean retrieved states of the scalar and vector models, respectively; Figs. 10(b) and (d) show the corresponding standard deviation. In these figures, solid lines indicate the results of the finer resolution models (226 channels for the scalar model and 452 channels for the vector model) and dash–dotted lines indicate the results of the coarser resolution models (44 channels for the scalar model and 88 channels for the vector model).

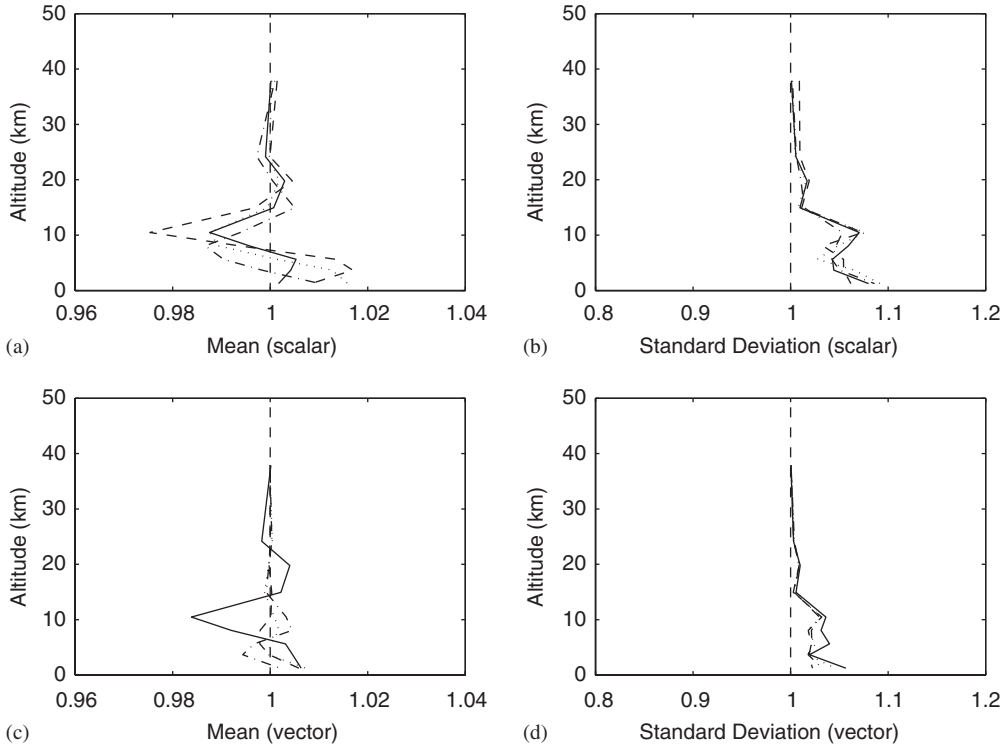

Fig. 9. Scaled profiles and standard deviation. The straight dashed line corresponds to the "true" state. (a) Mean retrieved states of the scalar model. (b) Standard deviation of the scalar model. (c) Mean retrieved state of the vector model. (d) Standard deviation of the vector model. In each plot, different line types show the results of different dust profiles. Solid line: standard dust profile; dashed line: annual mean dust profile; dash–dotted line: maximum dust profile; dotted line: minimum dust profile.

For the scalar model, the average retrieved ozone concentration from the coarser model has larger error in the troposphere, and the discrepancy between the "true" and retrieved states is as much as 4%. The standard deviation of the profiles does not change significantly, as seen in Fig. 10(b). For the vector retrieval, the mean retrieved states for the two cases are comparable to each other. However, in the troposphere, the model with fewer channels has a standard deviation two times as large as that of the finer model. Thus, we conclude that both SNR and number of channels are essential for this retrieval algorithm and more channels and higher SNR are preferred.

It is also interesting to point out that the 88 channel vector retrieval achieves similar accuracy as the 226 channel scalar retrieval. Both models have SNR = 1000. In other words, the coarser vector model with achievable SNR yields comparable results to a full scalar model with unrealistic SNR.

4. Results from information theory analysis

Deriving the atmospheric state from remote sensing measurements is an ill-posed problem, and as such, there are many different approaches to find a solution. Given a spectrum, it is prudent to ask how much information can be derived about the atmospheric state and if this is dependent upon prior knowledge. A formal description of the utility of a measurement can be gained by borrowing concepts from the fields of information theory and source coding and decoding. Rodgers suggests that the information content of a measurement can be defined qualitatively as the factor by which knowledge of a quantity is improved by making the measurement, and the degrees of freedom (DFS) evaluates the number of useful independent quantities that are present in the measurement [32].

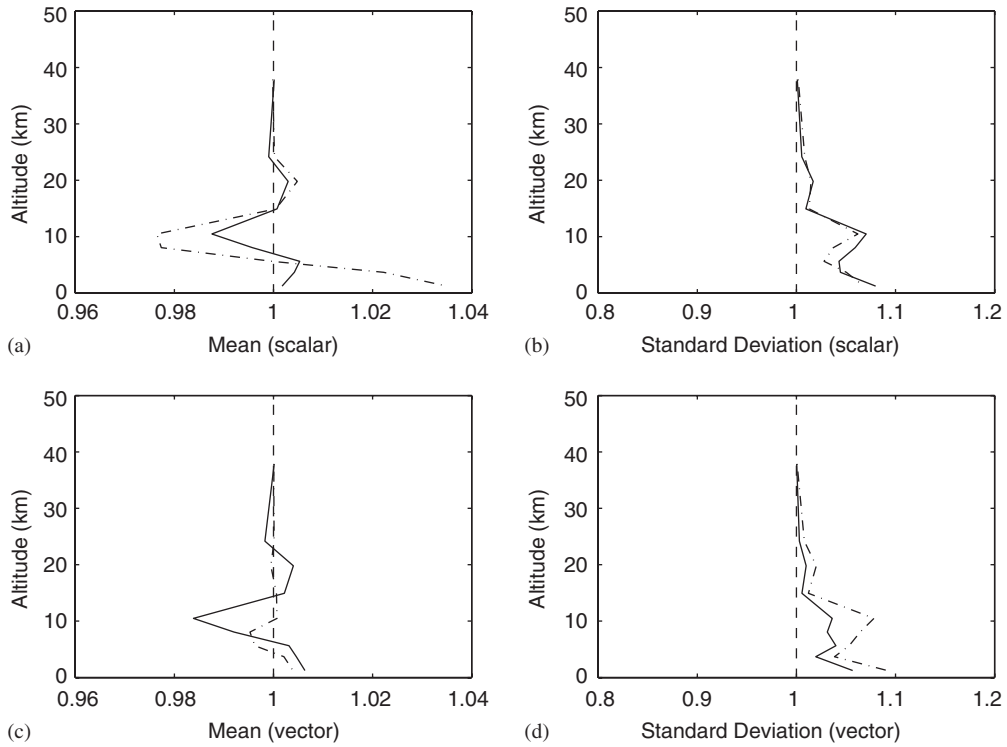

Fig. 10. Scaled profiles and standard deviation. The straight dashed line corresponds to the "true" state. (a) Mean retrieved states of the scalar model. (b) Standard deviation of the scalar model. (c) Mean retrieved state of the vector model. (d) Standard deviation of the vector model. In each plot, different line styles show the results of different models. Solid line: finer resolution model (226 channels for the scalar model and 452 for the vector model); dash–dotted line: coarser resolution model (44 channels for the scalar model and 88 for the vector model).

The utility of an information theoretical approach becomes apparent when making logistical choices about the retrieval for an atmospheric quantity. First, the information content and DFS of retrieval are, in general, independent of the coordinate system on which the retrieved state is defined (e.g. number of layers). Second, the total information content and DFS, if properly quantified, provide a metric by which the incorporation of the measurement into the updated state can be gauged. Therefore, one can optimize the retrieval according to this metric by making choices about instrument design, channel utilization, viewing geometry, etc. Optimization of retrieval performance with respect to other quantities, such as retrieval smoothness or minimum variance, is much less straightforward.

We calculate the DFS (d_s) and Shannon information content (H) according to Rodgers [32].

$$d_s = \mathrm{trace}\left(\left(\mathbf{K}^T\mathbf{S}_\varepsilon^{-1}\mathbf{K} + \mathbf{S}_a^{-1}\right)^{-1}\mathbf{K}^T\mathbf{S}_\varepsilon^{-1}\mathbf{K}\right), \tag{15}$$

$$H = -\frac{1}{2}\ln\left(\left|\left(\mathbf{K}^T\mathbf{S}_\varepsilon^{-1}\mathbf{K} + \mathbf{S}_a^{-1}\right)^{-1}\mathbf{S}_a^{-1}\right|\right). \tag{16}$$

Fig. 11 shows the DFS and the Shannon information content of the scalar (dashed line) and vector (solid line) models. H is scaled by ln(2) to show the information content in bits. The variation of DFS and H with SNR are shown in Figs. 11(a) and (b), respectively. The vector model gives roughly one additional DFS (20% enhancement) to the measurement. Similarly, 2–6 bits more information (15–20% enhancement) is obtained from the vector model. Both quantities illustrate the advantage of incorporating the measurement of the polarized component (only Q for this case) into the retrieval. Figs. 11(a) and (b) also suggest that for instruments with relatively high SNR, further improvement in the DFS and the Shannon information content

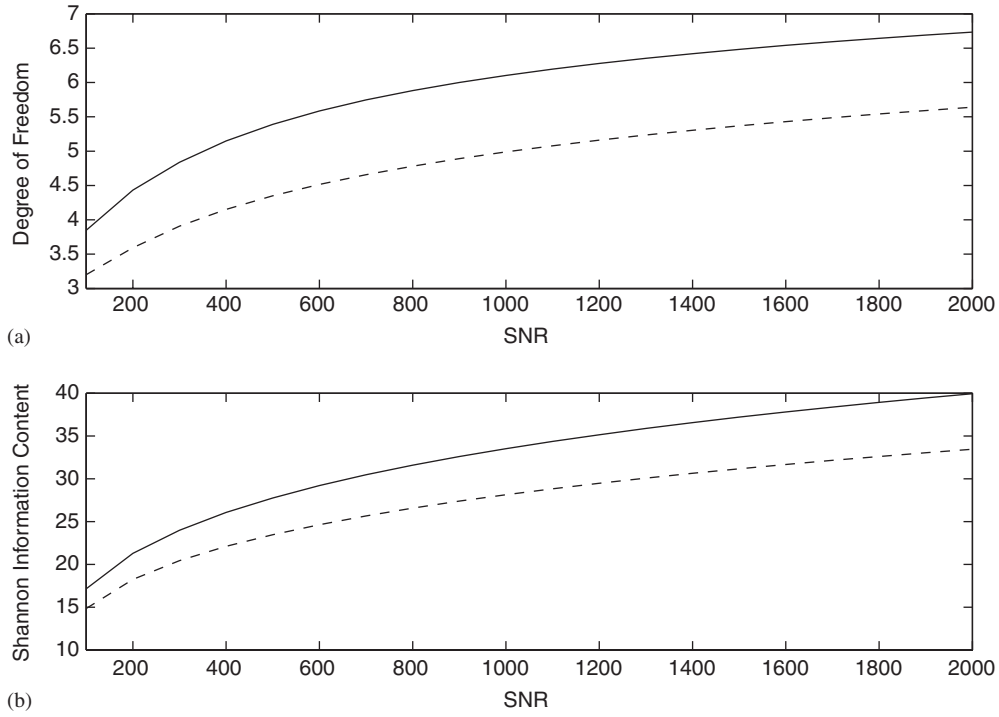

Fig. 11. (a) DFS versus SNR. Dashed line: scalar; solid line: vector. (b) Shannon information content (in bits) versus SNR. Dashed line: scalar; solid line: vector.

by minimizing noise is difficult to achieve. On the other hand, a large amount of additional information is available by including polarization in the measurement while maintaining the SNR. For the purpose of maximizing available information, measurement of the full Stokes vector is needed.

In order to verify the source of the extra information, we calculate the DFS and information content in the troposphere and stratosphere, separately. The increments after the introduction of polarization are shown in Fig. 12. The dashed and solid lines show the increase in the stratosphere and troposphere, respectively. From Fig. 12(a), it is clear that the increase in DFS in the troposphere is several times larger than that in the stratosphere. Similar behavior is found in the Shannon information content (Fig. 12(b)), except for very low SNR situations. We conclude that the inclusion of the polarized component significantly enhances information about the ozone state, especially in the troposphere. This is consistent with our discussion in Section 3.

5. Conclusion and discussion

We perform a retrieval of ozone number density profile from synthetic observations using the L–M iteration method based on optimal estimation theory. Our results show the capability of retrieving the ozone profile with this inverse algorithm, even in the presence of unknown random noise. By comparing the vector and scalar models, i.e. retrieval methods with and without polarization, we conclude that the vector model will significantly enhance the retrieval of ozone concentration, especially in the troposphere.

The relatively high concentration of the scattering species in the troposphere results in a significant polarization signature in the downwelling radiation. Hence, the measurement of other Stokes parameters in addition to the intensity will enhance tropospheric ozone retrieval. Our argument is reinforced by an information theoretical analysis. The degrees of freedom and the Shannon information content increase by roughly 20% if polarization is included in the retrieval algorithm. As expected, the information gain is larger in the troposphere.

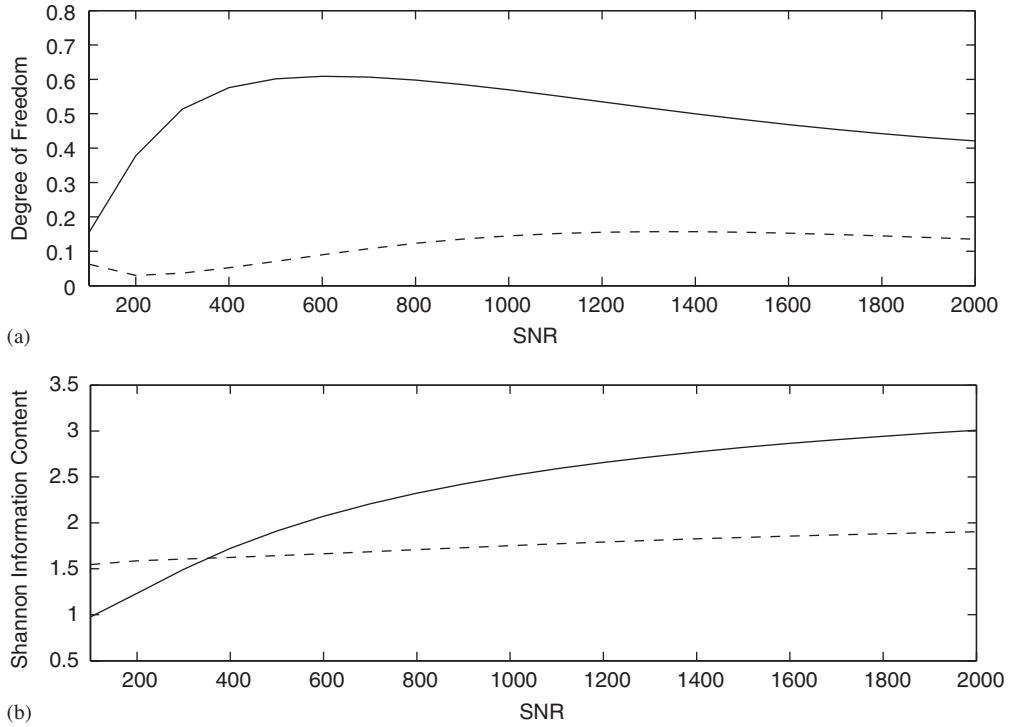

Fig. 12. DFS and Shannon information content (in bits) increment after introduction of polarization. (a) DFS increment versus SNR. Dashed line: stratosphere; solid line: troposphere. (b) Shannon information content increment (in bits) versus SNR. Dashed line: stratosphere; solid line: troposphere.

In order to focus on the effect of polarization, our synthetic retrieval is simplified and conducted with very specific parameterization and geometry. First, we assume that we know the temperature and aerosol profiles perfectly, which is unlikely to be true for a real retrieval. For the real cases, we need to obtain the simultaneous temperature profile since the ozone absorption cross section is very sensitive to temperature. We also need to retrieve the aerosol profile simultaneously since aerosol scattering influences the polarization. Such retrieval will increase the dimensionality of the state vector. Another assumption is that the SNR is uniform across the channels and for all Stokes parameters. For a grating spectrometer, the SNR is dependent on the number of incoming photons, and therefore depends on both wavelength and integration time. The SNR value we prescribed is very optimistic. Besides, the SNR for different Stokes parameters is likely to be different. In a real scenario, it is imperative to calibrate the instrument well and characterize the retrieval with the calibration. Nonetheless, our analysis sets baseline requirements necessary to achieve high retrieval precision. Finally, in order to optimize the detection and inversion, other viewing geometries should be investigated; efforts in this direction are currently underway. Different viewing geometries may provide higher SNR in shorter integration time, more information content and better sensitivity. However, they may also introduce some complexity to the instrument design and numerical modeling. Clearly, a thorough understanding of the physical and mathematical properties of the forward and inverse calculations is required for future retrieval, instrument design and mission planning.

Acknowledgements

We appreciate the helpful comments from J. Margolis, M. Newchurch, K. Chance, X. Liu, F. Mills, J. Herman, L. Li, X. Jiang, Y. Jiang, S. Herman, C. Kolb and two anonymous reviewers. This research is supported in part by NASA Grant NAG1-02081 and JPL Grant P421407 to California Institute of Technology.

References

[1] Goody RM, Yung YL. Atmospheric radiation: theoretical basis. New York: Oxford University Press; 1989.
[2] IPCC. Intergovernmental panel on climate change assessment: Climate change 1995, 1996, p. 73.
[3] Ramanathan V. Trace-gas greenhouse effect and global warming—underlying principles and outstanding issues—volvo environmental prize lecture—1997. Ambio 1998;27:187–97.
[4] Lacis AA, Webbles DJ, Logan JA. Radiative forcing of climate by changes in the vertical-distribution of ozone. J Geophys Res Atmosph 1990;95:9971–81.
[5] Wang WC, Yung YL, Lacis AA, Mo T, Hansen JE. Greenhouse effects due to man-made perturbations of trace gases. Science 1976;194:685–90.
[6] Wang WC, Pinto JP, Yung YL. Climatic effects due to halogenated compounds in the earths atmosphere. J Atmosp Sci 1980;37:333–8.
[7] Logan JA, Prather MJ, Wofsy SC, McElroy MB. Tropospheric chemistry—a global perspective. J Geophys Res Oceans Atmosph 1981;86:7210–54.
[8] Fusco AC, Logan JA. Analysis of 1970–1995 trends in tropospheric ozone at Northern Hemisphere midlatitudes with the GEOS-CHEM model. J Geophys Res Atmosph 2003;108:7–29.
[9] Marenco A, Gouget H, Nedelec P, Pages J-P. Evidence of a long-term increase in tropospheric ozone from Pic du Midu Data Series—consequences—positive radiative forcing. J Geophys Res 1994;99:16617–32.
[10] Wang Y, Jacob DJ. Anthropogenic forcing on tropospheric ozone and OH since preindustrial times. J Geophys Res 1998;103:31123–35.
[11] Mickley LJ, Jacob DJ, Rind D. Uncertainty in preindustrial abundance of tropospheric ozone: Implications for radiative forcing calculations. J Geophys Res 2001;106:3389–99.
[12] Götz FWP, Meetham AR, Dobson GMB. The vertical distribution of ozone in the atmosphere. Proc Roy Soc Lond 1934;145:416–46.
[13] DeLuisi JJ. Umkehr vertical ozone profile errors caused by the presence of stratospheric aerosols. J Geophys Res 1979;84:1766–70.
[14] DeLuisi JJ, Mateer CL, Bhartia PK. On the correspondence between Standard Umkehr, Short Umkehr, and solar backscattered ultraviolet ozone profiles. J Geophys Res 1985;90:3845–9.
[15] (WMO) WMO. Atmospheric ozone 1985, in *Global ozone research and monitoring project*, pp. 393–648.
[16] Jiang YB, Yung YL, Sander SP. Detection of tropospheric ozone by remote sensing from the ground. J Quant Spectrosc Radiat Transfer 1997;57:811–8.
[17] Hansen JE, Travis LD. Light scattering in planetary atmospheres. Space Sci Rev 1974;16:527–610.
[18] Hasekamp OP, Landgraf J. The need of polarization modeling for ozone profile retrieval from backscattered sunlight. J Geophys Res 2002;107:4692–704.
[19] Jiang YB, Yung YL, Sander SP, Travis LD. Modeling of atmospheric radiative transfer with polarization and its application to the remote sensing of tropospheric ozone. J Quant Spectrosc Radiat Transfer 2004;84:169–79.
[20] Chandrasekhar S. Radiative transfer. New York: Dover Publications; 1960.
[21] Hovenier JW. Multiple scattering of polarized light in planetary atmospheres. Astron Astrophys 1971;13:7–29.
[22] Hovenier JW, van der Mee CVM. Fundamental relationships relevant to the transfer of polarized light in a scattering atmosphere. Astron Astrophys 1983;128:1–16.
[23] Spurr RJD. Simultaneous derivation of intensities and weighting functions in a general pseudo-spherical discrete ordinate radiative transfer treatment. J Quant Spectrosc Radiat Transfer 2002;75:129–75.
[24] Spurr RJD. VLIDORT: A linearized pseudo-spherical vector discrete ordinate radiative transfer model for forward model and retrieval studies in multilayer, multiple scattering media. J Quant Spectrosc Radiat Transfer 2006, in press, doi:10.1016/j.jqsrt.2006.05.005.
[25] Natraj V, Spurr RJD, Jiang Y, Yung YL. Evaluation of errors from neglecting polarization in the forward modeling of O_2 A band measurements from space, with relevance to CO_2 column retrieval from polarization-sensitive instruments. J Spectrosc Radiat Transfer 2006, in press, doi:10.1016/j.jqsrt.2006.02.073.
[26] Coulson KL, Dave JV, Sekera Z. Tables related to radiation emerging from a planetary atmosphere with Rayleigh scattering. Berkeley: University of California Press; 1960.
[27] Siewert CE. A discrete-ordinates solution for radiative-transfer models that include polarization effects. J Quant Spectrosc Radiat Transfer 2000;64:227–54.
[28] Dave JV. Meaning of successive iteration of the auxiliary equation of radiative transfer. Astrophys J 1964;140:1292–303.
[29] Michelangeli DV, Allen M, Yung YL, Shia RL, Crisp D, Eluszkiewicz J. Enhancement of atmospheric radiation by an aerosol layer. J Geophys Res Atmosph 1992;97:865–74.
[30] Demerjian KL, Schere KL, Peterson JT. Theoretical estimates of actinic (spherically integrated) flux and photolytic rate constants of atmospheric species in the lower troposphere. Adv Environ Sci Technol 1980;10:369–459.
[31] Kuik K, de Haan JF, Hovenier JW. Benchmark results for single scattering by spheroids. J Quant Spectrosc Radiat Transfer 1992;47:477–89.
[32] Rodgers CD. Inverse methods for atmospheric sounding: theory and practice. Singapore: World Scientific Publishing Co. Pte. Ltd.; 2000.
[33] Dethof A, Holm EV. Ozone assimilation in the ERA-40 Reanalysis Project. Q J Roy Meteorol Soc 2004;130:2851–72.

[34] Lacis AA, Chowdhary J, Mishchenko MI, Cairns B. Modeling errors in diffuse-sky radiation: vector versus scalar treatment. Geophys Res Lett 1998;25:135–8.
[35] Yung YL, Jiang Y, Liao H, Gerstell MF. Enhanced UV penetration due to ozone cross-section changes induced by CO_2 doubling. Geophys Res Lett 1997;24:3229–31.
[36] Luo C, Mahowald NM, Corral Jd. Sensitivity study of meteorological parameters on mineral aerosol mobilization, transport, and distribution. J Geophys Res 2003;108:4447–67.